# Signatures of Chemical Dopants in Simulated Resonance Raman Spectroscopy of Carbon Nanotubes

Braden M. Weight,[1,2] Ming Zheng,[3] and Sergei Tretiak[2*]

[1]*Department of Physics and Astronomy, University of Rochester, Rochester, NY 14627, U.S.A*

[2]*Center for Integrated Nanotechnologies, Center for Nonlinear Studies, and Theoretical Division Los Alamos National Laboratory, Los Alamos, NM 87545, U.S.A.*

[3]*Materials Science and Engineering Division, National Institute of Standards and Technology, Gaithersburg, Maryland 20899, U.S.A.*

**ABSTRACT**

Single-walled carbon nanotubes (SWCNTs) with organic $sp^2$- or $sp^3$-hybdridization defects allow for robust tunability in many optoelectronic properties in these topologically interesting quasi-one-dimensional materials. Recent resonant Raman experiments have discovered new features in the intermediate frequency region upon functionalization and change with the degree of functionalization as well as with interactions between defect sites. In this letter, we report *ab initio* simulated near-resonant Raman spectroscopy results for pristine and chemically functionalized SWCNT models and find new features concomitant to experimental observations. We are able to assign the character of these features by varying the frequency of the external Raman laser frequency near the defect-induced $E_{11}^*$ optical transition using a perturbative treatment to the electronic structure of the system. Obtained insights establish relationships between nanotube atomistic structure and Raman spectra facilitating further exploration of SWCNTs with tunable optical properties tuned by chemical doping.

Email: serg@lanl.gov

Chemical control of surface modification in single-walled carbon nanotubes (SWCNTs) has recently taken a leap forward after developing new synthetic routes to functionalize SWCNTs with single-strand DNA (ssDNA)[1–3] wrapping, photochemistry utilizing singlet and triplet state pathways,[4,5] as well as well-established chemistries using diazonium salts, hypochlorite, and ozone functionalizations.[6–9] In all these cases, chemical doping creates a low-lying defect-associated $E_{11}^*$ exciton state below the fundamental $E_{11}$ exciton band of SWCNT that has improved optical properties and tunability. For example, in case of ssDNA wrapping, it is hypothesized that the guanine nucleotide base uniquely reacts with the SWCNT surface to form a $sp^3$- or $sp^2$-hybridiztion defect with complete control over the spacing between the adjacent defects and hence their inter-defect interactions and exciton delocalization properties. When utilizing photochemical routes, the photoexcited triplet pathway, in the absence of triplet-quenching oxygen species, has been shown to produce experimentally new atomistic configurations of defects expanding diversity of bonding configurations on the SWCNT lattice. SWCNT hybridization defects, in general, are known to break the symmetry of the system and introduce novel, redshifted, and localized excitons.[10–12] Similar functionalized systems using a variety of chemical adducts (*e.g.*, aryl, alkyl, etc.) have been well-studied both theoretically and experimentally. For example, the inductive effects of the chemical adduct [7,13–16] and long- and short-range defect-defect interactions.[17–19] on the energetically low-lying defect-associated $E_{11}^*$ exciton are shown to improve energetic tunability and capabilities for single-photon emission.[20–25] These studies have led to an increased understanding of these SWCNT systems and facilitated new experiments to deepen our understanding of these interesting topological materials.

Given a wide variety of possible defect configurations, identification of spectroscopic footprints of specific chemical groups bound to the tube surfaces, however, remains a challenge. For example, resonant Raman spectroscopy for functionalized SWCNTs has been reported but not well-decomposed and interpreted. These spectroscopic experiments are key to examining and explaining a great many things related to excited non-radiative dynamics relevant to non-linear spectroscopy[26–28] that include such processes as exciton trapping/de-trapping events at the defect sites,[17] or exciton-polariton dynamics involving defect states.[29] Our current work was inspired by two experimental studies on defected SWCNTs.[2,13] In both reports, $E_{22}$-resonant Raman spectra was performed on sets of defected SWCNTs when applying ssDNA[2] and aryl[13] functionalizations. In both cases, and as expected for any SWCNT sample, intensity of the primary defect-associated mode (D) was increased compared to that of the graphene-like mode (G) after surface functionalization. However, many interesting features in the intermediate regions of the Raman spectra between 300–1300 $cm^{-1}$ were observed[2] that may imply important features of these systems yet to be analyzed at the atomistic level. For example, these lower-energy modes may contribute to non-radiative relaxation processed involving transitions between excited states near the defect states that potentially can affect physical properties of the material.

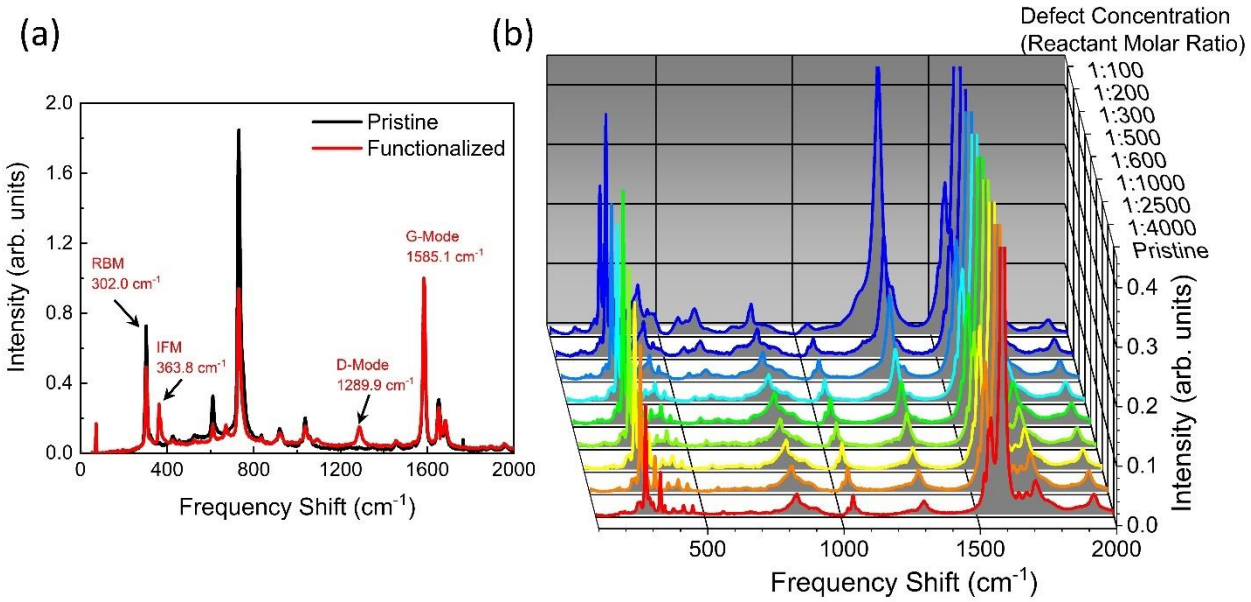


*Figure 1: (a) Pristine (black) and functionalized (red) (9,1) SWCNT resonant Raman spectra measured in experiment. Here, the resonance frequency was introduced at 1.85 eV near the $E_{22}$ band. The figure is plotted using raw data from Ref.* [2]*. (b) Resonant Raman spectroscopy for varied amounts of surface functionalization on (6,5) SWCNT with laser frequency set to 1.96 eV near the $E_{22}$ band as well. This figure is plotted using raw data from Ref.* [13]*.*

Fig. 1 showcases the two examples of resonant Raman spectra that form the inspiration and basis for this report. Fig. 1a presents $E_{22}$-resonant Raman spectra using data from the supporting information of ref. [2] indicating similar features upon functionalization with ssDNA-based functional guanine species on the (9,1) SWCNT chirality. Fig. 1b shows an experimental $E_{22}$-resonant Raman spectroscopy using data from ref. [13] varying the amount of diazonium-based defect concentration (axis into the page) on the (6,5) SWCNT chirality. In the region between the radial breathing mode (RBM, ~300 $cm^{-1}$) and the D-mode (~1300 $cm^{-1}$) – referred to as the intermediate frequency mode (IFM)[30–36] region – there are many peaks that change intensity with increasing defect concentration, most notably near 400 $cm^{-1}$, 600 $cm^{-1}$, and 1050 $cm^{-1}$. In both experiments, the IFM region was shown to be strongly influenced by the presence of the surface defects. Additionally, the spacing between adjacent guanine base units in the ssDNA strand[2] as well as the concentration of diazonium reagent[13] directly influence the intensity of the IFM peaks showing that the strengthened defect-defect interactions increase the intensity of these new modes with respect to the G-mode.

In this letter, we discuss theoretical simulations performed on the (9,1) SWCNT chirality to elucidate effects on simulated near-resonant Raman spectroscopy after functionalization using a perturbative treatment to the electronic structure of the material. In this way, we identify vibrational modes that can be interpreted as those stemming from the defect by varying the frequency of the external Raman laser near the $E_{11}^{*}$ transition.

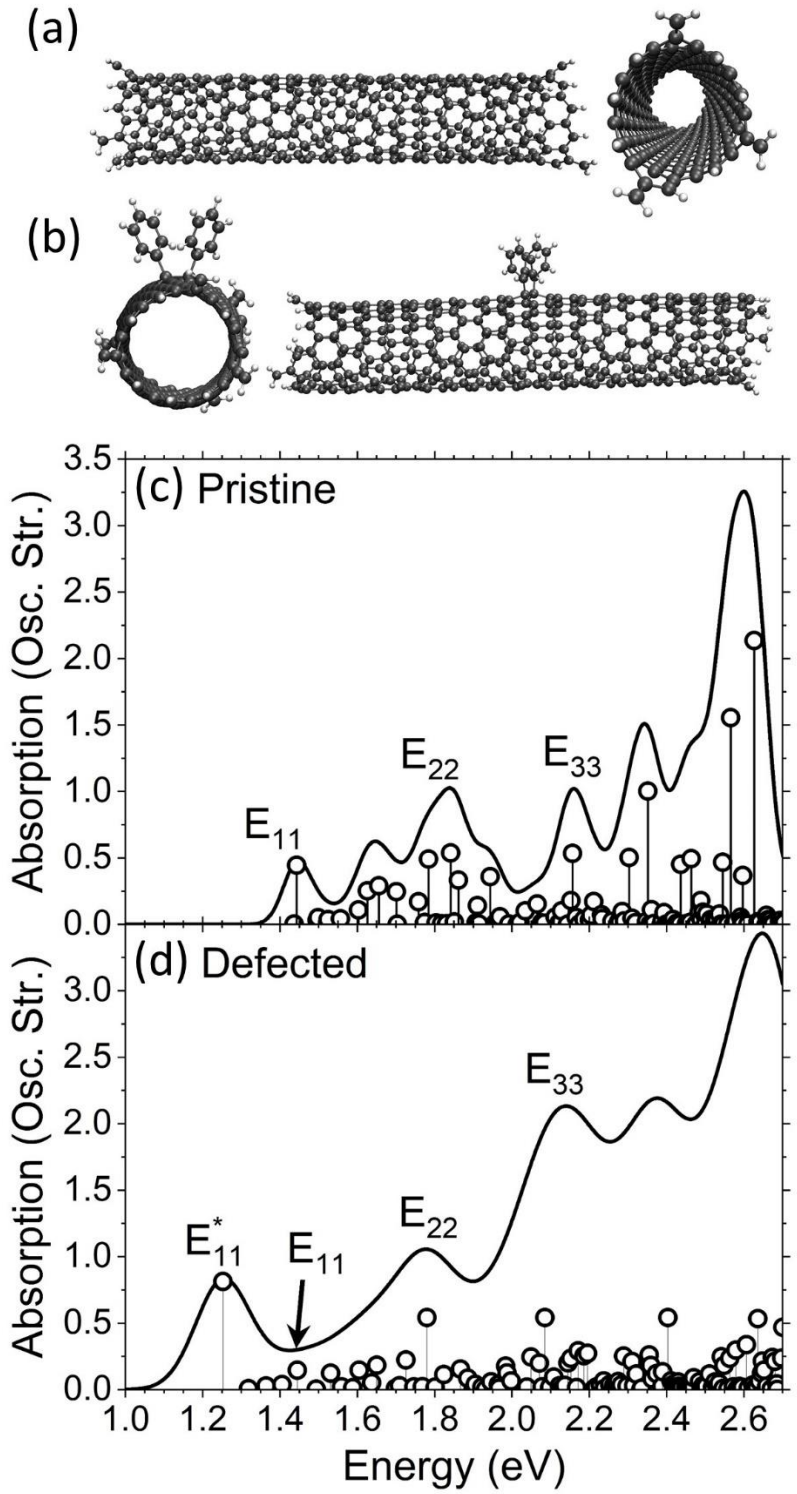


*Figure 2: (a,b) Pristine and Ortho(++) Aryl/Aryl defected (9,1) SWCNT structures used in this work. Computed absorption spectra for the (c) pristine and (d) defected (9,1) SWCNTs. The excitation energies were broadened by a Gaussian distribution with a width of 0.05 and 0.1 eV for the pristine and defected cases, respectively, for visual clarity.*

In order to rationalize the experimental findings, where a variety of SWCNT chiralities were examined, two (9,1) SWCNT models were chosen as the focus of our computational study. We expect our results to be easily transferable between chiralities, noting that the most important difference will be in the $E_{11}^*$ transition energy region, which is well-known from previous reports.[12] This allows us to choose the (9,1) SWCNT as our test case for the numerically intensive resonant Raman simulations. Fig. 2a,b shows the atomistic models of pristine and Ortho(++) aryl/aryl $sp^3$-defected SWCNTs (see Methods for explanation of defect and capping schemes). The calculated absorption spectra for the two SWCNT models are shown in Fig. 2c,d, which will be used later to motivate choices of perturbative Raman calculations. For the pristine case, one can find the corresponding major transitions seen in experiment $E_{11}$, $E_{22}$, and $E_{33}$ near to 1.45, 1.80, and 2.15 eV, respectively. The transition energies match very well to the reported experimental values.[37,38] For the defected case, the energies for each of the pristine transitions are only weakly modified, but the intensity of the $E_{11}$ transition becomes much reduced due to the presence of the defect. The $E_{11}^*$ transition appears at 1.25 eV with a redshift from the pristine $E_{11}$ of about 200 meV, which is consistent with previous similar calculations.[12]

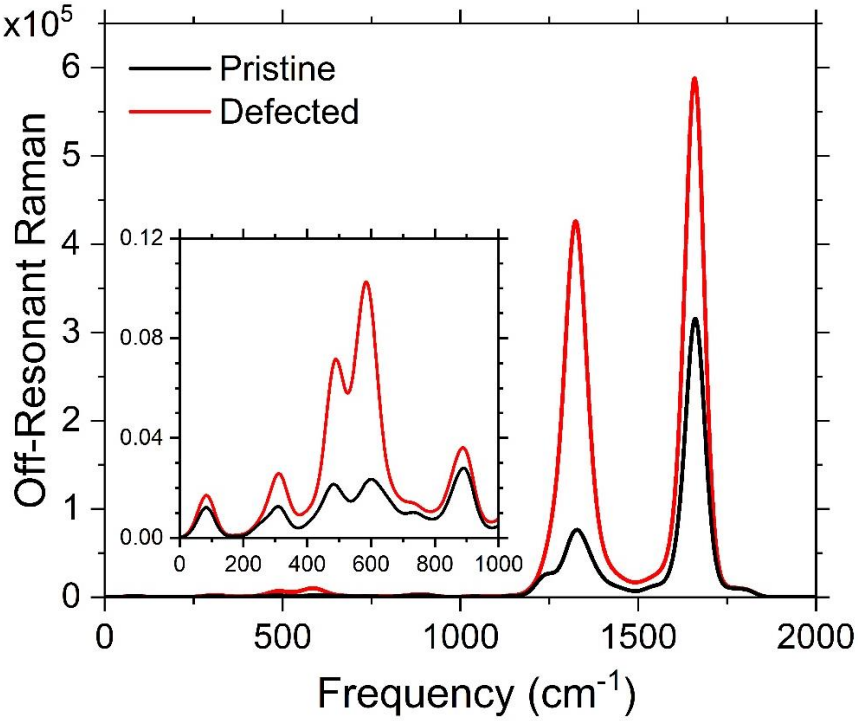


*Figure 3: Computed off-resonant Raman spectra for the pristine (black) and defected (red) SWCNT species. The inset shows a zoomed version of the 0 – 1000 $cm^{-1}$ region.*

Fig. 3 shows the off-resonant Raman spectra for the pristine (black) and defected (red) SWCNT models. The G- and D-bands are present in both the pristine and defected SWCNTs because of the finite SWCNT used for the modeling. The edges activate D-like Raman modes. However, upon functionalizing the SWCNT, the D-band increases sharply, indicating that the defect mode dominates the intensity of this band. Note that the G-band intensity is also increased as a result of functionalization; see Supporting Fig. S1 for normalized results with respect to the G-band peak

(which is commonly done in experiment). The inset shows the small perturbations to the low-frequency Raman modes induced by the defect. The modes around 500 and 600 $cm^{-1}$ are appreciably increased compared to the pristine system, but the total intensity is largely dominated by the G- and D-bands. In comparison to Fig. 1, the calculated off-resonant Raman spectra does not showcase the same interesting features recently explored by experiment. In this case, only the features present in the pristine SWCNT are modified (*i.e.*, increased in intensity).

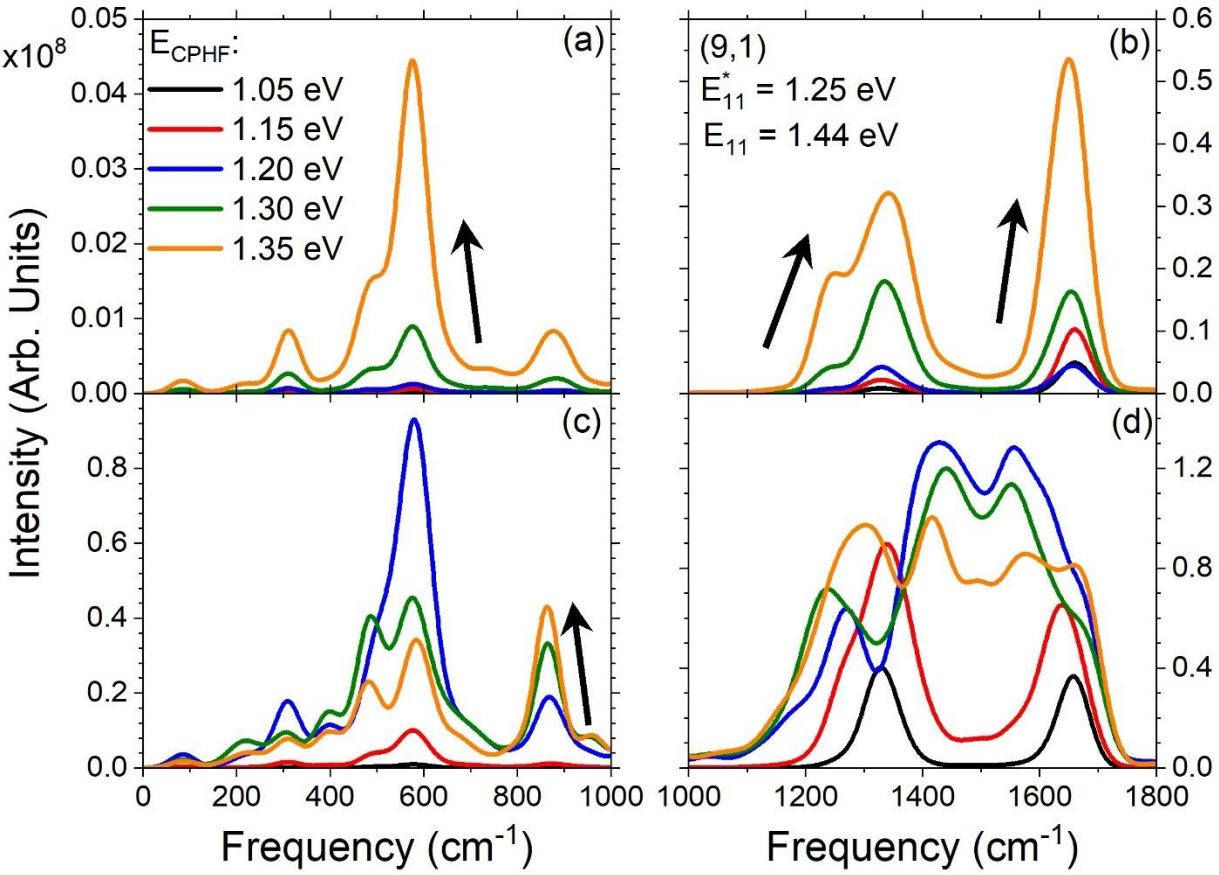


*Figure 4: Computed near-resonant Raman spectra at varying perturbative laser energies (colors) for the pristine (a,b) and defected (c,d) SWCNT models. The spectra are split into low-frequency (a,c) and high-frequency (b,d) regions for visual clarity. Note the variation in vertical scaling between all panels. The perturbation energies are all near the region of the computed $E_{11}^*$ transition of 1.25 eV. The arrows indicate monotonically varying trends with respect to increasing perturbative energy where applicable.*

To gain a more experimentally relevant understanding of the Raman intensities, we now examine simulated resonance Raman spectra utilizing the Coupled Perturbed Hartree-Fock (CPHF) approach (see Methods and Supporting Information). This technique can *directly examine effects originating from the resonant coupling of the laser field to electronic transitions*, which was done in experiment by coupling to the $E_{22}$ transition of the SWCNTs.[2,13] Compared to the off-resonant Raman spectra modeling (Fig. 3), the CPHF Raman spectra calculations are very expensive. We start with analysis of the Raman spectra near the $E_{11}^*$ transition of 1.25 eV at varying perturbative frequencies. Fig. 4a,b show pristine Raman spectra at five unique perturbative energies ($E_{CPHF}$): 1.05, 1.15, 1.20, 1.30, 1.35 eV. Note that the CPHF technique is unable to produce spectra exactly at or nearer to the $E_{11}^*$ transition energy due to extremely intense coupling which produces non-real-valued results in the computational software. Fig. 4c,d show the same calculations but with the ortho(++) Aryl/Aryl defected SWCNT. The spectra in each case are split between the low- (panels a,c) and high-frequency (panels b,d) ranges for visual clarity. The intensity-normalized version of this figure can be found in Supporting Fig. S2. The high-frequency pristine spectrum (Fig. 4b) at far-detuned perturbation frequency ($E_{CPHF}$ = 1.05 eV) shows vanishing intensity everywhere except a single peak at 1650 $cm^{-1}$ near the G-band of the computed off-resonant Raman spectrum for pristine system (Fig. 3). At less detuned CPHF frequencies, we see a systematic increase in the G-band as well as an increase in the D-band around 1350 $cm^{-1}$. We also note the presence of a lower-energy sideband to the D-mode appearing at 1250 $cm^{-1}$, which is also present in the off-resonant case (Fig. 3). The low-energy spectrum of the pristine system (Fig. 4a) showcases a monotonic (denoted as a black arrow) increase of three main bands at roughly 300, 600, and 900 $cm^{-1}$. Note the vertical scaling is an order of magnitude smaller than that for the high-frequency region. We will see later that these modes can be attributed primarily to activated edge modes of the system that are weakly coupled to the delocalized excitations in the pristine system (Fig. 2c). Some of these are optically dark but have non-zero oscillator strengths and may have strong overlap with the edge modes, which then contribute defect-like changes in their intensity.

Turning to the defect-associated spectra for the low-frequency region (Fig. 4c), we find that similar modes become activated as seen in the pristine system. However, the intensities of the modes are, in general, much larger and two of the three main modes at 300 and 600 $cm^{-1}$ undergo non-monotonic intensity changes (where the black arrows were removed in comparison to Fig. 4a). This strongly contrasts the pristine case due to the introduction of the defect $E_{11}^*$ transition at 1.25 eV. The mode near 850 $cm^{-1}$ is monotonically raising with increasing CPHF energy, indicating that this mode may couple to the intermediate-energy dark exciton states with non-zero edge character, which will be revisited later. The mode near 600 $cm^{-1}$ reaches a maximum at a $E_{CPHF}$ = 1.20 eV frequency (blue) with a very weak lower-energy sideband at 450 $cm^{-1}$. The higher-frequency CPHF calculations (green, $E_{CPHF}$ = 1.30 eV; orange, $E_{CPHF}$ = 1.35 eV) show decreasing intensity with increasing energetic detuning from the $E_{11}^*$ transition. Similarly, the farthest negatively detuned calculation at $E_{CPHF}$ = 1.05 eV (black) has vanishing intensity, and the second-most negatively detuned (red, $E_{CPHF}$ = 1.15 eV) shows only the main band at 600 $cm^{-1}$. The sidebands around 450 $cm^{-1}$ are most dominant at $E_{CPHF}$ = 1.30 and $E_{CPHF}$ = 1.35 eV frequencies. The mode at 300 $cm^{-1}$ also shows the same trends as the 600-$cm^{-1}$ mode but with smaller intensity. These two modes at 300 and 600 $cm^{-1}$ originate from the $sp^3$-defect located at the center of the SWCNT and demonstrate that these intermediate energy frequencies (200 – 700 $cm^{-1}$) are enhanced in the experimental resonant Raman spectra due to $sp^3$-lattice defects. However, the

mode near 800 $cm^{-1}$ seems to be edge-dominated. However, as we will see later, it competes with modes at similar frequencies localized to the center of the SWCNT that dominate the intensity.

Fig. 4d shows the high-frequency CPHF Raman spectrum for the defected case. For the highly detuned, low-frequency calculation at $E_{CPHF}$ = 1.05 eV (black) and the next nearest point at $E_{CPHF}$ = 1.15 eV (red), the off-resonant D- and G-bands are recovered. Interestingly, the D-band intensity dominates over the G-band intensity. For the $E_{CPHF}$ = 1.20, 1.30, and 1.35 eV calculations, two new main modes are introduced between the D- and G-band peaks near 1450 and 1550 $cm^{-1}$. This parallels the complete disappearance of the D- and G-peaks for the 1.20 and 1.30 eV cases. Moving from $E_{CPHF}$ = 1.05 to 1.30 eV, we see shifts in both the frequency and intensity of a new sideband to the D-band peak, starting near 1300 $cm^{-1}$ for $E_{CPHF}$ = 1.05 eV, and ending near 1200 $cm^{-1}$ for $E_{CPHF}$ = 1.30 eV. The $E_{CPHF}$ = 1.35 eV spectrum is rather unique compared to the others, in a sense that it reflects coupling to both the $E_{11}^{*}$, intermediate dark, and $E_{11}$ electronic transitions. This gives both the new intermediate (between D- and G-modes) and the D- and G-modes themselves modified features distinctly different from that in the off-resonant Raman spectra. These observations contrast changes seen in the pristine case. Likely, the new modes between the D- and G-bands originate from the high-frequency C-H oscillations[39] near or on the defect and become enhanced only during this $E_{11}^{*}$ coupling, which is not done is experiment and therefore not seen.

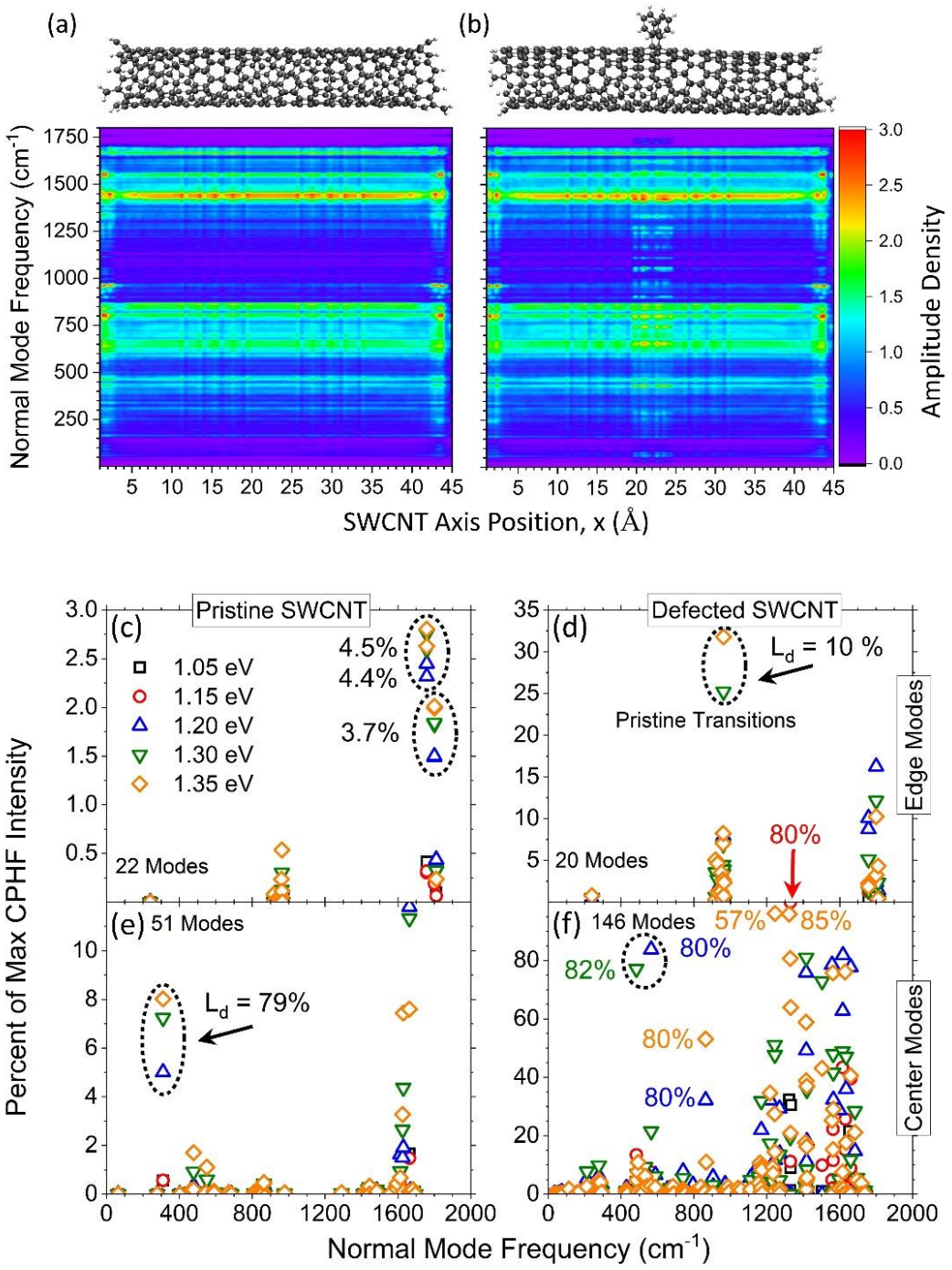


*Figure 5: (a,b) Amplitude density map of the normal mode plotted as a function of SWCNT axis position, x, and frequency for the (a) pristine and (b) defected SWCNT models. The probability amplitudes are convolved with a Gaussian function of width $\sigma$ = 5 cm$^{-1}$. (c-f) Percent CPHF maximum intensity of normal modes localized to within (c, d) 5 Å of the edges by 35 % and (e, f) to the center 10 Å by 30 % of the (c, e) pristine and (d, f) defected SWCNT models for all CPHF perturbation energies. The number of modes that fall inside the criteria are shown in each panel. Note the differences in vertical scales between all four panels. In all panels, some points are labeled by their $L_d$ (%) value as the percent normal mode extent along the SWCNT axis.*

To better understand the character of the modes activated by resonance effects, one can decompose the normal modes based on their contributions at each point along the SWCNT main axis. Supporting Fig. S3 provides a visualization of the position-resolved probability amplitudes for each normal mode (Eq. S15 in Supporting Information) for (a) pristine and (b) defected SWCNT models. Various types of mode localizations can be seen: (I) edge-localized, (II) defect-(center-)localized, and (III) delocalized. This depiction in a form of a 2D heatmap is shown in Supporting Fig. S4. Further, taking these discrete probability distributions and convolving with a finite-width Gaussian function in the frequency domain (Eq. S17 in Supporting Information), one obtains an amplitude density map shown in Fig. 5a,b. The pristine (Fig. 5a) and defected (Fig. 5b) SWCNT maps show large differences in the central region of the SWCNT axis, indicating the presence of the defect-localized modes. A 3D contour map is shown for visual clarity in Supporting Fig. S5 using the same data as in Fig. 5b. Finally, the difference amplitude density between the pristine and defected density maps is shown in Supporting Fig. S6, indicating the contributions coming directly from the defect modes (see additional discussion in the Supporting Information).

Moving to more quantitative descriptions of the mode character, an effective localization parameter – also referred to as the inverse participation ratio[14,40–42] $L_d$, can be computed for each normal mode (Eq. S18 in Supporting Information), and this data is presented overlayed upon the same data as presented in Fig. 4 and can be found in Supporting Fig. S7. The localization of the normal modes ranges widely from near 10 % (indicating a spatial localization to 10 % of the SWCNT axis) to near 90 % (nearly delocalized case across the entire SWCNT) for both the pristine (Fig. S7a) and defected (Fig. S7b) SWCNT models. The $L_d$ parameter provides a quantitative measure of the normal mode extent along the SWCNT axis and will be used to help understand and partition the normal modes into quantifiable classes of SWCNT modes.

From the spatially resolved probabilities (Eq. 3), we further define the first two classes of modes – (I) and (II) from above – as the modes with greater than (I) 35 % edge character and greater than (II) 30 % center character, respectively (see Supporting Information for additional details). The intensity of these modes is then plotted for each external laser frequency as the percent of the maximum intensity for each frequency. Fig. 5c-f showcase the results for edge-localization (Fig. 5c,d) and center localization (Fig. 5e,f) for the pristine (Fig. 5c,e) and defected (Fig. 5d,f) SWCNT models. Notably, with this criterion, there are 22 and 20 modes with edge character for pristine and defected cases, respectively. The intensity of these modes in the pristine system is less than 3 % while in the defected model, some modes are present around 30 % (~900 $cm^{-1}$) with the larger laser frequencies ($E_{CPHF}$ = 1.30 and 1.35 eV). This evidences that stronger coupling to the more delocalized excitonic states activates the edge modes that appear as mostly dark excitonic states in the absorption spectrum for the defected SWCNT (Fig. 2d). These states with edge character exhibit a small feature in the near-resonant Raman spectrum (Fig. 4a,c) for the pristine and defected cases that becomes more intense with increasing CPHF frequency. These mostly dark excitonic states mediate the coupling to activate these edge modes (see Supporting Fig. S8 for the real-space projected transition density isosurfaces of the lowest five excitonic transitions in the defected model). The edge-localized mode near 1800 $cm^{-1}$ should exhibit some features in Fig. 4b, but the Gaussian broadening eliminates them due to the large density of features at lower frequencies. As such, these are not resolved in the spectra for the Gaussian width $\sigma$ = 25 $cm^{-1}$.

The center-localized modes in the pristine SWCNT model (Fig. 5e) exhibit two main features at ~300 and 1650 $cm^{-1}$ with up to 12 % CPHF Raman intensity compared to the maximum. The defected model, Fig. 5f, showcases three times as many center-character modes with additional features at 500, 600 and 850 $cm^{-1}$ with a band of activations between the frequencies 1200 – 1600 $cm^{-1}$ with CPHF Raman intensity up to 100% compared to the maximum for the modes in the 1200 – 1600 $cm^{-1}$ range for all external laser frequencies, except for the strongly detuned $E_{CPHF}$ = 1.05 eV frequency. The overlapping-in-frequency modes that are edge- and center-localized near 300, 500, and 900 $cm^{-1}$ become washed out once the defect states are activated. This analysis has shown that although the edge modes can be activated through resonant coupling, the center-localized, defect-induced modes dominate the spectrum for all choices of external laser frequencies and therefore weakly participating edge modes largely do not affect the above conclusions. Thus, we have proved validity of our model for analyzing the modes activated by resonant Raman spectroscopy in experiment.

For completeness, Supporting Fig. S9 shows pre-resonance Raman spectra for two additional CPHF energies: 1.45 eV (panel a) and 1.75 eV (panel b). These energies are near to the computed $E_{11}$ (1.44 eV) and $E_{22}$ (1.78 eV) excited state transitions of the system. In both cases, the systems exhibit a largely delocalized Raman intensity distribution. Notably, the D- and G-bands from the off-resonance Raman have completely disappeared, and a new peak at 1500 $cm^{-1}$ is present both in the pristine and defected cases at both perturbation energies. The low-frequency range exhibits a broad set of peaks centered around 600 $cm^{-1}$ as seen in the Fig. 4c; however, nearly all adjacent modes have now been enhanced through coupling to the electronic transitions of pristine tube. Supporting Fig. S10 displays an alternative depiction of the intensity through an intensity-difference function ($\Delta I = I^{DEF} - I^{PRISTINE}$). These features are stemming from coupling many modes along the SWCNT axis to the bright $E_{11}$ and $E_{22}$ transition with strong oscillator strengths, as well as to all other semi-bright excitations nearby in energy. This effectively washes out the small details pointed out in the above section while coupling to the weaker transition with low number of nearby-in-energy excitons (*i.e.*, low density of states). However, there are a couple important facets to these high-frequency calculations: Unexpectedly, the CPHF method results in an intensity decrease near the G-mode frequencies (~1500 $cm^{-1}$) for the $E_{11}$ coupling (Fig. S9a), where usually the CPHF approach would yield an overwhelming intensity increase when coupling to such a bright transition. This may be due to the reduction in oscillator strength of the $E_{11}$ exciton after placement of the defect (Fig. 2c,d). One important implications of this work is as follows: modifying the external laser frequency results in drastic changes to the Raman spectra obtained through coupling to nearby bright and semi-bright electronic transitions. In experiment, often this tunability remains unexplored (*i.e.*, often only coupling to the $E_{22}$ transition is investigated). However, this additional control may give rise to different spectra for the same molecular system even at slightly different incident light frequencies. This is to say, coupling only to the $E_{22}$ bright transition may not be providing the entire story, as additional electronic frequencies may activate new Raman modes and provide valuable additional information.

In summary, this letter reports results of *ab initio* simulations elucidating recent experimental resonant Raman spectroscopy data in chemically functionalized SWCNT species. These experiments pointed to additional Raman modes becoming activated after functionalization in multiple SWCNT chiralities. Our simulations showcase similar new features in near-resonant Raman spectra that have not been reported or explained before with atomistic simulations to the

best of our knowledge. We attribute these new features to those vibrational modes, which are strongly coupled to the defect-associated optical transition ($E_{11}^*$) due to the unique and pointed changes to these modes using varying incident laser frequencies near the $E_{11}^*$ transition. We envision that this work will inspire more intricate future investigations – both experimental and theoretical – exploring the physical nature of these intermediate modes strongly coupled to the defect-associated excitonic transitions. Additionally, we suggest future studies to focus on the effects of multiple localized defects as well as modifications due to the adduct's chemical identity, which will lead to further tunability of non-radiative relaxation pathways explorable with resonant Raman spectroscopy analysis. With this new information, the community at large can devise ways to utilize these lower-energy vibrational modes to probe excitonic dynamics and devise new chemistries on SWCNT lattices.

## Methods

*Geometry and Electronic Structure*

The pristine (9,1) SWCNT was constructed with a single unit cell of length ~ 4 nm, and its edges were capped with three methylene groups, which has been previously shown to recover the semi-infinite electronic structure of the SWCNTs.[12,43,44] An aryl/aryl $sp^3$-hybridization defect was formed on the surface by covalently attaching two aryl radicals to adjacent (i.e., *ortho*) carbons in a single ring in the Ortho(++) configuration, which is defined as the *ortho* bond that lies approximately 5.2 degrees away from the SWCNT axis. These defect configurations have been well-defined in previous computational reports for this and other chirlaities.[10,12,14,15,45]

All geometries were optimized in the ground state electronic state at the density functional theory (DFT) level using the B3LYP functional and STO-3G basis. Similar functionals and basis sets have been previously shown to provide qualitatively accurate electronic structure energies and excitonic localization properties of these systems.[10,12,14,15,45] The lowest 150 singlet excited states were computed for each system at the minimum of the ground state potential energy surface using linear-response time-dependent DFT (TD-DFT) using the same functional and basis. The real-space projected transition density was generated with the aid of the MultiWfn package.[46]

All ground, excited, and perturbative electronic structure calculations were performed using the Gaussian 2016 software package.[47]

## Supporting Information

Supporting figures to the main figures can be found indicating normalized Raman spectra and excitonic transition density isosurfaces as well as additional figures depicting the normal mode analysis performed. Further, a general outline of the coupled perturbed Hartree-Fock equations and a detailed explanation of the normal mode analysis can also be found.

## Acknowledgements

All authors kindly thank YuHuang Wang for providing the experimental resonance Raman data found in Fig. 1b. This work was supported by the Los Alamos National Laboratory (LANL)

Directed Research and Development funds (LDRD) and performed in part at the Center for Integrated Nanotechnologies (CINT), a U.S. Department of Energy, Office of Science User Facility. For computational support, the authors thank the Center for Integrated Research Computing (CIRC) at the University of Rochester as well as the LANL Institutional Computing for providing computational resources and technical support.

## References

(1) Zheng, Y.; Bachilo, S. M.; Weisman, R. B. Controlled Patterning of Carbon Nanotube Energy Levels by Covalent DNA Functionalization. *ACS Nano* **2019**, *13* (7), 8222–8228. https://doi.org/10.1021/acsnano.9b03488.

(2) Lin, Z.; Beltran, L. C.; De los Santos, Z. A.; Li, Y.; Adel, T.; Fagan, J. A.; Hight Walker, A. R.; Egelman, E. H.; Zheng, M. DNA-Guided Lattice Remodeling of Carbon Nanotubes. *Science* **2022**, *377* (6605), 535–539. https://doi.org/10.1126/science.abo4628.

(3) Zheng, Y.; Alizadehmojarad, A. A.; Bachilo, S. M.; Weisman, R. B. Guanine-Specific Chemical Reaction Reveals SsDNA Interactions on Carbon Nanotube Surfaces. *J. Phys. Chem. Lett.* **2022**, 2231–2236. https://doi.org/10.1021/acs.jpclett.2c00030.

(4) Zheng, Y.; Han, Y.; Weight, B. M.; Lin, Z.; Gifford, B. J.; Zheng, M.; Kilin, D.; Kilina, S.; Doorn, S. K.; Htoon, H.; Tretiak, S. Photochemical Spin-State Control of Binding Configuration for Tailoring Organic Color Center Emission in Carbon Nanotubes. *Nat Commun* **2022**, *13* (1), 4439. https://doi.org/10.1038/s41467-022-31921-0.

(5) Zheng, Y.; Bachilo, S. M.; Weisman, R. B. Photoexcited Aromatic Reactants Give Multicolor Carbon Nanotube Fluorescence from Quantum Defects. *ACS Nano* **2020**, *14* (1), 715–723. https://doi.org/10.1021/acsnano.9b07606.

(6) Ghosh, S.; Bachilo, S. M.; Simonette, R. A.; Beckingham, K. M.; Weisman, R. B. Oxygen Doping Modifies Near-Infrared Band Gaps in Fluorescent Single-Walled Carbon Nanotubes. *Science* **2010**, *330* (6011), 1656–1659. https://doi.org/10.1126/science.1196382.

(7) Kwon, H.; Furmanchuk, A.; Kim, M.; Meany, B.; Guo, Y.; Schatz, G. C.; Wang, Y. Molecularly Tunable Fluorescent Quantum Defects. *J. Am. Chem. Soc.* **2016**, *138* (21), 6878–6885. https://doi.org/10.1021/jacs.6b03618.

(8) He, X.; Kevlishvili, I.; Murcek, K.; Liu, P.; Star, A. [2π + 2π] Photocycloaddition of Enones to Single-Walled Carbon Nanotubes Creates Fluorescent Quantum Defects. *ACS Nano* **2021**, *15* (3), 4833–4844. https://doi.org/10.1021/acsnano.0c09583.

(9) Lin, C.-W.; Bachilo, S. M.; Zheng, Y.; Tsedev, U.; Huang, S.; Weisman, R. B.; Belcher, A. M. Creating Fluorescent Quantum Defects in Carbon Nanotubes Using Hypochlorite and Light. *Nat Commun* **2019**, *10* (1), 2874. https://doi.org/10.1038/s41467-019-10917-3.

(10) Gifford, B. J.; Kilina, S.; Htoon, H.; Doorn, S. K.; Tretiak, S. Exciton Localization and Optical Emission in Aryl-Functionalized Carbon Nanotubes. *J. Phys. Chem. C* **2018**, *122* (3), 1828–1838. https://doi.org/10.1021/acs.jpcc.7b09558.

(11) Gifford, B. J.; Kilina, S.; Htoon, H.; Doorn, S. K.; Tretiak, S. Controlling Defect-State Photophysics in Covalently Functionalized Single-Walled Carbon Nanotubes. *Acc. Chem. Res.* **2020**, *53* (9), 1791–1801. https://doi.org/10.1021/acs.accounts.0c00210.

(12) Gifford, B. J.; Saha, A.; Weight, B. M.; He, X.; Ao, G.; Zheng, M.; Htoon, H.; Kilina, S.; Doorn, S. K.; Tretiak, S. Mod(n-m,3) Dependence of Defect-State Emission Bands in Aryl-

Functionalized Carbon Nanotubes. *Nano Lett.* **2019**, *19* (12), 8503–8509. https://doi.org/10.1021/acs.nanolett.9b02926.
(13) Piao, Y.; Meany, B.; Powell, L. R.; Valley, N.; Kwon, H.; Schatz, G. C.; Wang, Y. Brightening of Carbon Nanotube Photoluminescence through the Incorporation of Sp 3 Defects. *Nat. Chem.* **2013**, *5* (10), 840–845. https://doi.org/10.1038/nchem.1711.
(14) Weight, B. M.; Gifford, B. J.; Tretiak, S.; Kilina, S. Interplay between Electrostatic Properties of Molecular Adducts and Their Positions at Carbon Nanotubes. *J. Phys. Chem. C* **2021**, *125* (8), 4785–4793. https://doi.org/10.1021/acs.jpcc.0c10157.
(15) Gifford, B. J.; He, X.; Kim, M.; Kwon, H.; Saha, A.; Sifain, A. E.; Wang, Y.; Htoon, H.; Kilina, S.; Doorn, S. K.; Tretiak, S. Optical Effects of Divalent Functionalization of Carbon Nanotubes. *Chem. Mater.* **2019**, *31* (17), 6950–6961. https://doi.org/10.1021/acs.chemmater.9b01438.
(16) Weight, B.; Sifain, A.; Gifford, B.; Htoon, H.; Tretiak, S. On-the-Fly Non-Adiabatic Dynamics Simulations of Single-Walled Carbon Nanotubes with Covalent Defects. **2022**. https://doi.org/10.26434/chemrxiv-2022-chjjw.
(17) Zheng, Y.; Weight, B. M.; Jones, A. C.; Chandrasekaran, V.; Gifford, B. J.; Tretiak, S.; Doorn, S. K.; Htoon, H. Photoluminescence Dynamics Defined by Exciton Trapping Potential of Coupled Defect States in DNA-Functionalized Carbon Nanotubes. *ACS Nano* **2021**, *15* (1), 923–933. https://doi.org/10.1021/acsnano.0c07544.
(18) Wu, X.; Kim, M.; Qu, H.; Wang, Y. Single-Defect Spectroscopy in the Shortwave Infrared. *Nat. Commun.* **2019**, *10* (1), 1–7. https://doi.org/10.1038/s41467-019-10788-8.
(19) Weight, B. M.; Sifain, A. E.; Gifford, B. J.; Kilin, D.; Kilina, S.; Tretiak, S. Coupling between Emissive Defects on Carbon Nanotubes: Modeling Insights. *J. Phys. Chem. Lett.* **2021**, *12* (32), 7846–7853. https://doi.org/10.1021/acs.jpclett.1c01631.
(20) Endo, T.; Ishi-Hayase, J.; Maki, H. Photon Antibunching in Single-Walled Carbon Nanotubes at Telecommunication Wavelengths and Room Temperature. *Appl. Phys. Lett.* **2015**, *106* (11), 113106. https://doi.org/10.1063/1.4915618.
(21) He, X.; Hartmann, N. F.; Ma, X.; Kim, Y.; Ihly, R.; Blackburn, J. L.; Gao, W.; Kono, J.; Yomogida, Y.; Hirano, A.; Tanaka, T.; Kataura, H.; Htoon, H.; Doorn, S. K. Tunable Room-Temperature Single-Photon Emission at Telecom Wavelengths from Sp3 Defects in Carbon Nanotubes. *Nature Photon* **2017**, *11* (9), 577–582. https://doi.org/10.1038/nphoton.2017.119.
(22) Jeantet, A.; Chassagneux, Y.; Raynaud, C.; Roussignol, Ph.; Lauret, J. S.; Besga, B.; Estève, J.; Reichel, J.; Voisin, C. Widely Tunable Single-Photon Source from a Carbon Nanotube in the Purcell Regime. *Phys. Rev. Lett.* **2016**, *116* (24), 247402. https://doi.org/10.1103/PhysRevLett.116.247402.
(23) Kawabe, R.; Takaki, H.; Ibi, T.; Maeda, Y.; Nakagawa, K.; Maki, H. Pure and Efficient Single-Photon Sources by Shortening and Functionalizing Air-Suspended Carbon Nanotubes. *ACS Appl. Nano Mater.* **2020**, *3* (1), 682–690. https://doi.org/10.1021/acsanm.9b02209.
(24) Ma, X.; Hartmann, N. F.; Baldwin, J. K. S.; Doorn, S. K.; Htoon, H. Room-Temperature Single-Photon Generation from Solitary Dopants of Carbon Nanotubes. *Nat. Nanotechnol.* **2015**, *10* (8), 671–675. https://doi.org/10.1038/nnano.2015.136.

(25) Nutz, M.; Zhang, J.; Kim, M.; Kwon, H.; Wu, X.; Wang, Y.; Högele, A. Photon Correlation Spectroscopy of Luminescent Quantum Defects in Carbon Nanotubes. *Nano Lett.* **2019**, *19* (10), 7078–7084. https://doi.org/10.1021/acs.nanolett.9b02553.
(26) Gao, B.; Hartland, G. V.; Huang, L. Transient Absorption Spectroscopy and Imaging of Individual Chirality-Assigned Single-Walled Carbon Nanotubes. *ACS Nano* **2012**, *6* (6), 5083–5090. https://doi.org/10.1021/nn300753a.
(27) Park, J.; Deria, P.; Therien, M. J. Dynamics and Transient Absorption Spectral Signatures of the Single-Wall Carbon Nanotube Electronically Excited Triplet State. *J. Am. Chem. Soc.* **2011**, *133* (43), 17156–17159. https://doi.org/10.1021/ja2079477.
(28) Styers-Barnett, D. J.; Ellison, S. P.; Mehl, B. P.; Westlake, B. C.; House, R. L.; Park, C.; Wise, K. E.; Papanikolas, J. M. Exciton Dynamics and Biexciton Formation in Single-Walled Carbon Nanotubes Studied with Femtosecond Transient Absorption Spectroscopy. *J. Phys. Chem. C* **2008**, *112* (12), 4507–4516. https://doi.org/10.1021/jp7099256.
(29) Lüttgens, J. M.; Berger, F. J.; Zaumseil, J. Population of Exciton–Polaritons via Luminescent Sp3 Defects in Single-Walled Carbon Nanotubes. *ACS Photonics* **2021**, *8* (1), 182–193. https://doi.org/10.1021/acsphotonics.0c01129.
(30) Zaumseil, J.; Jakubka, F.; Wang, M.; Gannott, F. In Situ Raman Mapping of Charge Carrier Distribution in Electrolyte-Gated Carbon Nanotube Network Field-Effect Transistors. *J. Phys. Chem. C* **2013**, *117* (49), 26361–26370. https://doi.org/10.1021/jp409849w.
(31) Inaba, T.; Tanaka, Y.; Konabe, S.; Homma, Y. Effects of Chirality and Defect Density on the Intermediate Frequency Raman Modes of Individually Suspended Single-Walled Carbon Nanotubes. *J. Phys. Chem. C* **2018**, *122* (16), 9184–9190. https://doi.org/10.1021/acs.jpcc.8b01017.
(32) Dresselhaus, M. S.; Jorio, A.; Hofmann, M.; Dresselhaus, G.; Saito, R. Perspectives on Carbon Nanotubes and Graphene Raman Spectroscopy. *Nano Lett.* **2010**, *10* (3), 751–758. https://doi.org/10.1021/nl904286r.
(33) Fantini, C.; Jorio, A.; Souza, M.; Ladeira, L. O.; Souza Filho, A. G.; Saito, R.; Samsonidze, Ge. G.; Dresselhaus, G.; Dresselhaus, M. S.; Pimenta, M. A. One-Dimensional Character of Combination Modes in the Resonance Raman Scattering of Carbon Nanotubes. *Phys. Rev. Lett.* **2004**, *93* (8), 087401. https://doi.org/10.1103/PhysRevLett.93.087401.
(34) Fantini, C.; Jorio, A.; Souza, M.; Saito, R.; Samsonidze, Ge. G.; Dresselhaus, M. S.; Pimenta, M. A. Steplike Dispersion of the Intermediate-Frequency Raman Modes in Semiconducting and Metallic Carbon Nanotubes. *Phys. Rev. B* **2005**, *72* (8), 085446. https://doi.org/10.1103/PhysRevB.72.085446.
(35) Skákalová, V.; Maultzsch, J.; Osváth, Z.; Biró, L. P.; Roth, S. Intermediate Frequency Modes in Raman Spectra of Ar+-Irradiated Single-Wall Carbon Nanotubes. *physica status solidi (RRL) – Rapid Research Letters* **2007**, *1* (4), 138–140. https://doi.org/10.1002/pssr.200701069.
(36) Luo, Z.; Papadimitrakopoulos, F.; Doorn, S. K. Intermediate-Frequency Raman Modes for the Lower Optical Transitions of Semiconducting Single-Walled Carbon Nanotubes. *Phys. Rev. B* **2007**, *75* (20), 205438. https://doi.org/10.1103/PhysRevB.75.205438.
(37) Bachilo, S. M.; Strano, M. S.; Kittrell, C.; Hauge, R. H.; Smalley, R. E.; Weisman, R. B. Structure-Assigned Optical Spectra of Single-Walled Carbon Nanotubes. *Science* **2002**, *298* (5602), 2361–2366. https://doi.org/10.1126/science.1078727.

(38) Weisman, R. B.; Bachilo, S. M. Dependence of Optical Transition Energies on Structure for Single-Walled Carbon Nanotubes in Aqueous Suspension: An Empirical Kataura Plot. *Nano Lett.* **2003**, *3* (9), 1235–1238. https://doi.org/10.1021/nl034428i.
(39) Chen, Y.-J.; Chen, H.-L.; Young, T.-F.; Chang, T.-C.; Tsai, T.-M.; Chang, K.-C.; Zhang, R.; Chen, K.-H.; Lou, J.-C.; Chu, T.-J.; Chen, J.-H.; Bao, D.-H.; Sze, S. M. Hydrogen Induced Redox Mechanism in Amorphous Carbon Resistive Random Access Memory. *Nanoscale Research Letters* **2014**, *9* (1), 52. https://doi.org/10.1186/1556-276X-9-52.
(40) Murphy, N. C.; Wortis, R.; Atkinson, W. A. Generalized Inverse Participation Ratio as a Possible Measure of Localization for Interacting Systems. *Phys. Rev. B* **2011**, *83* (18). https://doi.org/10.1103/PhysRevB.83.184206.
(41) Wegner, F. Inverse Participation Ratio in 2 + e Dimensions. *Z. Physik B Cond. Mat.* **1980**, *36* (3), 209–214. https://doi.org/10.1007/BF01325284.
(42) Kilina, S.; Batista, E. R.; Yang, P.; Tretiak, S.; Saxena, A.; Martin, R. L.; Smith, D. L. Electronic Structure of Self-Assembled Amorphous Polyfluorenes. *ACS Nano* **2008**, *2* (7), 1381–1388. https://doi.org/10.1021/nn800204m.
(43) Sharma, A.; Gifford, B. J.; Kilina, S. Tip Functionalization of Finite Single-Walled Carbon Nanotubes and Its Impact on the Ground and Excited State Electronic Structure. *J. Phys. Chem. C* **2017**, *121* (15), 8601–8612. https://doi.org/10.1021/acs.jpcc.7b00147.
(44) Kilina, S.; Tretiak, S. Excitonic and Vibrational Properties of Single-Walled Semiconducting Carbon Nanotubes. *Advanced Functional Materials* **2007**, *17* (17), 3405–3420. https://doi.org/10.1002/adfm.200700314.
(45) Weight, B. M.; Sifain, A. E.; Gifford, B. J.; Kilin, D.; Kilina, S.; Tretiak, S. Coupling between Emissive Defects on Carbon Nanotubes: Modeling Insights. *J. Phys. Chem. Lett.* **2021**, *12* (32), 7846–7853. https://doi.org/10.1021/acs.jpclett.1c01631.
(46) Lu, T.; Chen, F. Multiwfn: A Multifunctional Wavefunction Analyzer. *J. Comput. Chem.* **2012**, *33* (5), 580–592. https://doi.org/10.1002/jcc.22885.
(47) Frisch, M. J.; Trucks, G. W.; Schlegel, H. B.; Scuseria, G. E.; Robb, M. A.; Cheeseman, J. R.; Scalmani, G.; Barone, V.; Petersson, G. A.; Nakatsuji, H.; Li, X.; Caricato, M.; Marenich, A. V.; Bloino, J.; Janesko, B. G.; Gomperts, R.; Mennucci, B.; Hratchian, H. P.; Ortiz, J. V.; Izmaylov, A. F.; Sonnenberg, J. L.; Williams; Ding, F.; Lipparini, F.; Egidi, F.; Goings, J.; Peng, B.; Petrone, A.; Henderson, T.; Ranasinghe, D.; Zakrzewski, V. G.; Gao, J.; Rega, N.; Zheng, G.; Liang, W.; Hada, M.; Ehara, M.; Toyota, K.; Fukuda, R.; Hasegawa, J.; Ishida, M.; Nakajima, T.; Honda, Y.; Kitao, O.; Nakai, H.; Vreven, T.; Throssell, K.; Montgomery Jr., J. A.; Peralta, J. E.; Ogliaro, F.; Bearpark, M. J.; Heyd, J. J.; Brothers, E. N.; Kudin, K. N.; Staroverov, V. N.; Keith, T. A.; Kobayashi, R.; Normand, J.; Raghavachari, K.; Rendell, A. P.; Burant, J. C.; Iyengar, S. S.; Tomasi, J.; Cossi, M.; Millam, J. M.; Klene, M.; Adamo, C.; Cammi, R.; Ochterski, J. W.; Martin, R. L.; Morokuma, K.; Farkas, O.; Foresman, J. B.; Fox, D. J. *Gaussian 16 Rev. C.01*; Wallingford, CT, 2016.